Journal of King Saud University – Science (2015) **27**, 76–91

King Saud University
Journal of King Saud University – Science
www.ksu.edu.sa
www.sciencedirect.com

ORIGINAL ARTICLE

Preparation and characterization of novel $CuBi_2O_4/SnO_2$ p–n heterojunction with enhanced photocatalytic performance under UVA light irradiation

Elaziouti Abdelkader [a,b,*], **Laouedj Nadjia** [a,b], **Bekka Ahmed** [a]

[a] *LCMIA, Laboratory, Faculty of Sciences, University of the Science and the Technology of Oran (USTO M.B), BP 1505 El M'naouar, 31000 Oran, Algeria*
[b] *Dr. Moulay Tahar University, Saida, Algeria, BP 138 Route Mascara, Saida 20000, Algeria*

Received 19 February 2014; accepted 18 June 2014
Available online 7 July 2014

KEYWORDS

$CuBi_2O_4/SnO_2$ heterostructure;
z-scheme photocatalysis system;
Congo red;
Photocatalytic activity;
Band theory;
Synergy effect

Abstract A novel p-$CuBi_2O_4$/n-SnO_2 heterostructure photocatalyst with different mass ratios was synthesized by the solid state technique, and characterized by X-ray diffraction (XRD), scanning electron microscopy (SEM) and UV–Vis diffuse reflectance spectroscopy (DRS). The photocatalytic activities of p-$CuBi_2O_4$/n-SnO_2 photocatalysts were assessed based on the photodegradation of Congo red (CR) dye as a probe reaction under UVA (365 nm) light irradiation. Experimental results showed that the phase composition, surface morphology of particles, and optical absorption of the sample were found to vary significantly with the mass ratios and pH medium. The p-$CuBi_2O_4$/n-SnO_2 photocatalyst exhibited higher photocatalytic performance as compared with $CuBi_2O_4$ and SnO_2. The photodegradation reactions were satisfactory correlated with the pseudo-first-order kinetic model. The optimum amount of doped $CuBi_2O_4$ was 5 wt% as a result of 58.06% of photoactivity of CR within 100 min under UVA light at pH = 8 and 25 °C, which is about 2 times higher than that of pure SnO_2. On the basis of the calculated energy band positions and the active species

* Corresponding author at: LCMIA, Laboratory, Faculty of Sciences, University of the Science and the Technology of Oran (USTO M.B), BP 1505 El M'naouar, 31000 Oran, Algeria.
E-mail addresses: elaziouti_a@yahoo.com (E. Abdelkader), nlaouedj@yahoo.fr (L. Nadjia), bekka_ahmed@yahoo.com (B. Ahmed).

Peer review under responsibility of King Saud University.

ELSEVIER Production and hosting by Elsevier

http://dx.doi.org/10.1016/j.jksus.2014.06.002

during photocatalytic process, the mechanism of the enhanced photocatalytic activity was discussed by solid state z-scheme photocatalysis system.

1. Introduction

Advanced oxidation processes are of great scientific and practical interest in terms of ecology and sustainable development (Fujishima and Honda, 1972; Zhang and Zhu, 2005). The heterogeneous photocatalysis of organic pollutants on semiconductor surfaces has attracted much attention as a 'green' technique. Most researches consider heterogenic systems based on TiO_2 (Degussa P25, Hombriat UV-100, Aldrich, etc.) owing to their high photocatalytic activity and stability as well as their widespread uses for large-scale water treatment (Wang et al., 2006a,b). However, the intrinsic band gap of TiO_2 is 3.2 eV, which requires the excitation wavelength < 387.5 nm. It is a major disadvantage of TiO_2 using as a photocatalyst working under visible light ($\geqslant 420$ nm). The high rate of electron–hole recombination often results in a low quantum yield and poor efficiency of photocatalytic reactions. In order tomeet the requirement of future environment and energy technologies, it is necessary to develop highly efficient, non toxic andchemically stable photocatalyst. Semiconductor catalysts such as TiO_2 (Xiaoning et al., 2011), SnO_2 (Sangami and Dharmaraj, 2012), ZrO_2 (Karunakaran et al., 2009) CeO_2 (Yongchuan et al., 2014), Fe_2O_3 (Seiji and Toshiyuki, 2009), Bi_2O_3 (Zhong et al., 2011), Sb_2O_3 (Arham et al., 2011), WO_3 (Fumiaki et al., 2013) and ZnO (Vora et al., 2009) metal oxides and CdS (Chae et al., 2010;), CdSe (Frame et al., 2008) CdTe (Kovalenko et al., 2004), ZnS (Karunakaran et al., 2009), PbS (Wang et al., 2011) and HgS (Rengaraj et al., 2014) metal chalcogenides have long been investigated for environmental applications. However, their practical uses have been constrained by their low photocatalytic activity under solar light, short-term stability against photo- and chemical corrosion as well as potential toxicity.

SnO_2, with a wide band gap of 3.6 eV at 300 K (Derbal et al., 2008), is known as n-type semiconductor and exhibits excellent optical, electrical and chemical properties and high thermal stability. Research has shown that the semiconductor SnO_2 material has wide potential applicabilities such as solid-state gas sensors (Ying et al., 2004), transparent conducting electrodes (Chopra et al., 1983), rechargeable Li batteries and optical electronic devices (Aoki and Sasakura, 1970). The tin dioxide (SnO_2) has low cost and toxicity, in addition to high availability. This oxide is among the few with the band gap energy near to visible light (Yang et al., 2006; Zhang et al., 2006). During the past decade, SnO_2 nanostructures have been one of the most important oxide nanostructures due to their properties and potential application (Cheng et al., 2004). Recently its composites have been studied as promising semiconductors in the photocatalytic decoloration of wastewaters (Xi et al., 2008; Wang et al., 2006a,b; Nayral et al., 2000; Mukhpadhyay et al., 2000; Teeramongkonrasmee and Sriyudthsak, 2000). Although photocatalytic activity of SnO_2 has intensively been investigated, the broad band gap energy and the electronic potential position in the conductance and valence bands of this material seriously limit its further application as a photocatalyst utilizing solar energy (Li et al., 2009).

Various strategies in the liquid-phase system have been adopted for size-controlled synthesis of various functional nanomaterials, including transition metal doping (Couselo et al., 2008), noble metal deposition (Sasahara et al., 2006) doping non-metallic elements (Geng et al., 2008), doping transition metal surface photosensitization (Mora-Sero et al., 2007) and coupled polycrystallites or colloidal semiconductors (Bian et al., 2008). Thus, the combination of semiconductor has become a hot topic among researchers in the last decade to improve the photostimulated electron–hole separation and effectively inhibit their recombination. The major characteristic of this technique is to assemble a heterojunction interface between wide and narrow band gap semiconductors with matching energy band potentials. In this way, electric field assisted transportation of charges from one particle to the other through interfaces is favorable for the electron–hole separations in the composite materials, and thus the electron and hole transfer from catalyst to adsorbed substrate can be obtained (Li and Yan, 2009; Liu et al., 2010a,b). The extensive search published on n–n type junction semiconductor systems were mostly focused on SnO_2-based photocatalyst materials, such as ZnO/SnO_2 (Wang et al., 2002), Fe_2O_3/SnO_2 (Zhuang et al., 2008), $SrNb_2O_6/SnO_2$ (Xinping et al., 2008), TiO_2-SnO_2/Fe^{+3} (Sikong et al., 2010), La2O3/SnO_2 (Xia et al., 2006), Ag_3PO_4/SnO_2 (Zhang et al., 2011), RGO/SnO_2 (Zhang et al., 2012), Nb_6O_{17}/SnO_2 (Wang et al., 2010a,b), TiO_2/SnO_2 (Hou et al., 2007; Sasikala et al., 2009), CeO_2/SnO_2 (Foletto et al., 2012), Cr_2O_3/SnO_2 (Bhosale et al., 2013), and so on. The results showed that nearly all the n–n junction composite semiconductors exhibited better photocatalytic properties than single ones. However, to the best of our knowledge, the use of the p–n type composite semiconductors has been rarely reported in the literature and only few examples of the p–n junction photocatalysts, such as CuO/SnO_2 (Xia et al., 2007), $CuFeO_2/SnO_2$ (Derbal et al., 2008), and NiO/SnO_2 (n-SnO_2 p-Si (Yang et al., 2009; Wang et al. 2010a,b; Mohamed and Aazam, 2012), have been studied. Theoretically, when p-type semiconductor and n-type semiconductor are connected to each other, the micro p–n heterojunction composite semiconductors will be formed; the inner electric field will also be produced in the interface. Once optical excitation occurs, a free electron (e^-) and an electronic vacancy (a hole, h^+) are formed, separated and migrated effectively in a semiconductor being partially localized on structural defective centers of its crystalline lattice, hence improving the electrical properties of semiconductor.

In this investigation, we have studied the photocatalytic efficiency of a p-$CuBi_2O_4$/n-SnO_2 composite, in which SnO_2 was associated with Bismuth Cuprites ($CuBi_2O_4$) to form p–n heterojunction composite semiconductors in different mass ratios. $CuBi_2O_4$ was chosen as a sensitizer semiconductor due to its narrow band gap energy of 1.5 eV (Arai et al., 2007; Liu et al., 2010a,b). $CuBi_2O_4$ is well-known as an excellent host

matrix for luminescent materials due to its low phonon energy, high visible-light responsiveness and adequate thermal stability. It functions as a sensitizer by the absorption of UV light to yield an excited state in the heterojunction composite semiconductors of p-$CuBi_2O_4$/n-SnO_2, which may increase the probability of light-generated carrier transfer and hence reduces the recombination of photogenerated electrons and holes substantially improving the photocatalytic properties.

So, the aim of this study is to clarify the photocatalytic efficiency of this novel p–n type composite semiconductor p-$CuBi_2O_4$/n-SnO_2 prepared by a physical mixing process through doping $CuBi_2O_4$ into SnO_2 matrix. The as-prepared p-$CuBi_2O_4$/n-SnO_2 nanoparticles were characterized by a number of techniques such as X-ray diffraction (XRD), scanning electron microscopy (SEM) and UV–visible diffuse reflectance spectroscopy (DRS). The photocatalytic degradation of Congo red (CR) dye under UV light irradiation was investigated over nanosized photocatalyst p-$CuBi_2O_4$/n-SnO_2 at different operating parameters such as, amount of doped $CuBi_2O_4$ and pH solution. The experimental data were quantified by applying the pseudo-first order kinetic model. Mechanisms of the increase in the photocatalytic activity were also investigated through a solid state z-scheme photocatalysis system, which mimics the z-scheme in the natural photosynthesis of green plants.

2. Experimental

2.1. Chemical reagents

The starting materials used in the synthesis: α-Bi_2O_3 (99.99%), CuO (99.99%) and SnO_2 (99.99%) were all obtained from Aldrich chemical company Ltd. Congo red (C.I. 22020, MW = 696.67 g mol^{-1}, $C_{32}H_{24}N_6O_6S_2{\cdot}2Na$, λ_{max} = 497 nm and pKa = 4) and other chemicals used in the experiments (NH_4OH and H_2SO_4) were purchased from C.I.S.A. Espagne. Distilled water was used for the preparation of various solutions.

2.2. Preparation of p-$CuBi_2O_4$

The p-$CuBi_2O_4$ powder was prepared according to the previously reported procedure (Arai et al., 2007; Liu et al., 2010a,b; Elaziouti et al., 2012). α-Bi_2O_3 and CuO were used as starting materials. The stoichiometric proportion mixture of Bi_2O_3 and CuO was previously ground for a period of time in an agate mortar, and then heated at the rate of 5 °C/min in a muffle oven (Linn High Therm) and thermally treated at 750 °C for 72 h in air. After the muffle oven was naturally cooled to room temperature, the black $CuBi_2O_4$ powder was ground in the agate mortar and then was collected as the precursor to prepare the composite photocatalyst p-$CuBi_2O_4$/n-SnO_2.

2.3. Preparation of semiconductor p-$CuBi_2O_4$/n-SnO_2

Combined semiconductors $CuBi_2O_4$/SnO_2 were prepared by a physical milling technique. Different $CuBi_2O_4$/SnO_2 powder samples were prepared in a ratio (mass concentration) of 5%, 10%, 20%, 30%, 40% and 50% respectively, by varying the amount of $CuBi_2O_4$ and subsequently milled in the agate mortar for 30 min. The final samples were used for the determination of characterization and photocatalytic activity.

2.4. Characterization

Phase evolution and crystalline of the resulting powders were characterized by X-ray diffraction (XRD) in an automatic D8 Bruker AXS diffractometer using CuKα radiation (λ = 1.5406 Å). XRD diffractogrammes were collected in 10–70° intervals with a scan speed of 10°/min. The crystallite average size (d_{DRX}) calculation using the Scherrer (Pullar et al., 1988) equation is as follows (Eq. 1):

$$d_{DRX} = \frac{0.9\lambda}{\beta \sin\theta} \quad (1)$$

where $\beta = \sqrt{(FWHM)^2 - (0.3)^2}$ and λ is the X-ray wavelength (1.5406 Å). FWHM is the full-width at half maximum and θ is the Bragg angle. FWHM was calculated from the peak having the highest intensity in all the samples. The lattice constants of the samples calculated from their corresponding XRD pattern data are obtained by Fullprof program. The crystallite sizes of the pure nanoparticles were deduced from the XRD patterns by calculation of the Scherrer equation.

Scanning electron microscopy (SEM) (Hitachi S-4800 N) is used to characterize the morphology of the particles.

UV–Vis diffuse reflectance spectroscopy measurements were carried out using a Perkin Elmer Lambda 650 spectrophotometer equipped with an integrating sphere attachment. The analysis range was from 200 to 900 nm, and polytetrafluoroethylene (PTFE, Teflon) was used as a reflectance standard.

The residual RC concentrations during the course of degradation were monitored with UV mini-1240 Spectrophotometer (Shimadzu UV mini-1240) in the range 200–800 nm, using 1 cm optical pathway cells.

2.5. Photocatalytic study measurements

The photodegradation of CR catalyzed by the p-$CuBi_2O_4$/n-SnO_2 samples was investigated under UVA light irradiation. 100 mg of catalyst was suspended in a CR solution (200 mL, 20 mg/L) in quartz cell tube. The suspension pH value was previously adjusted at 8 using $NaOH/H_2SO_4$ solutions using a (Hanna HI 210) pH meter. Prior to UV light irradiation, the suspension was stirred with magnetic stirrer (Speedsafe™ Hanna) for 30 min under dark conditions at 298 K to ensure the establishment of adsorption/desorption equilibrium between the catalyst and CR. The sample was then irradiated at 298 K using 6 W ultraviolet (λ = 365 nm, BLX-E365) photoreactor under continuous stirring. As the reaction proceeded, a 5 ml suspension was taken at 20 min intervals during the catalytic reaction and was centrifuged using centrifuge (EBA-Hetlich) at 3500 rpm for 15 min to completely remove photocatalyst particles. The residual RC concentrations during the course of degradation were monitored with a UV mini-1240 Spectrophotometer (Shimadzu UV mini-1240) in the range 200–800 nm, using 1 cm optical pathway cells.

The effect of initial pH on the photocatalytic degradation of CR only was conducted from pH 6–12 for avoiding dye aggregation. Data obtained from the photocatalytic degradation experiments were then used to calculate the degradation efficiency η′ (%) of the substrate (Eq. 2):

$$\eta'(\%) = \left[\frac{(C_i - C_f)}{C_i}\right] 100 \quad (2)$$

where C_i: dye initial concentration (mg L^{-1}) and C_f: dye residual concentration after certain intervals (mg L^{-1}).

According to Planck's Law and some further calculation, we can find that the absorption wavelength of the photoreactor can be calculated by determining its band gap value (Eq. 3):

$$E_g = \frac{1239\ \text{eV . nm}}{\lambda} \quad (3)$$

where h is Planck's constant ($4.13566733 \times 10^{-15}$ eV s); c is the speed of light ($2.99792458 \times 10^{17}$ nm/s) and λ is the UVA-light wavelength (355–375 nm).

From the calculation, in order to absorb a UVA-light wavelength, the band gap value of the photoreactor has to be below 3.49 eV and above 3.30 eV.

The photocatalytic degradation efficiency of catalyst for the degradation CR was quantified by the measurement of dye apparent first order rate constants under operating parameters. Surface catalyzed reactions can often be adequately described by a monomolecular Langmuir–Hinshelwood mechanism, in which an adsorbed substrate with fractional surface coverage θ is consumed at an initial rate given as follows (Eq. 4) (Vasanth Kumar et al., 2008):

$$-\left[\frac{dC}{dt}\right] = r_0 = K_{app}\ \theta = \frac{K_1 K_2 C_0}{1 + K_1 C_0} \quad (4)$$

where K_1 is a specific rate constant that changes with photocatalytic activity, K_2 is the adsorption equilibrium constant, and C_0 is the initial concentration of the substrate. Inversion of the above rate equation is given by Eq. (5):

$$\frac{1}{K_{app} C_0} = \frac{1}{K_1 K_2} + \frac{C_0}{K_1} \quad (5)$$

Thus, a plot of reciprocal of the apparent first order rate constant $1/K_{app}$ against initial concentration of the dye C_0 should be a straight line with a slope of $1/K_1$ and an intercept of $1/K_1K_2$. Such analysis allows one to quantify the photocatalytic activity of catalyst through the specific rate constant K_1 (with larger K_1 values corresponding to higher photocatalytic activity) and adsorption equilibrium constant K_2 (K_2 expresses the equilibrium constant for fast adsorption–desorption processes between surface of catalyst and substrates). The integrated form of the above equation (Eq. (5)) yields the following Eq. (6):

$$t = \frac{1}{K_1 K_2} \ln \frac{C_0}{C} + \frac{1}{K_2}(C_0 - C) \quad (6)$$

where t is the time in minutes required for the initial concentration of the dye C_0 to decrease to C. Since the dye concentration is very low, the second term of the expression becomes small when compared with the first one and under these conditions the above equation reduces to Eq. (7):

$$\ln \frac{C_0}{C} \approx K_1 K_2 t = K_{app} t \quad (7)$$

where K_{app} is the apparent pseudo-first order rate constant, C and C_0 are the concentration at time 't' and 't = 0', respectively. The plot of ln C_0/C against irradiation time t should give straight lines, whose slope is equal to K_{app}.

The half-life of dye degradation at various process parameters was raised from Eq. (8):

$$t_{1/2} = \frac{0.5 C_0}{K_2} + \frac{0.693}{K_1 K_2} \quad (8)$$

where half-life time, $t_{1/2}$, is defined as the amount of time required for the photocatalytic degradation of 50% of CR dye in a aqueous solution by catalyst.

3. Results and discussions

3.1. XRD analysis of (*x* wt%) $CuBi_2O_4/SnO_2$ Nanocomposites

Fig. 1, shows the XRD patterns of the as-synthesized (5 wt%) $CuBi_2O_4/SnO_2$ nanocomposites in comparison with those of $CuBi_2O_4$ precursor and pure SnO_2. Diffraction peaks of pure SnO_2 (Fig. 1a) at 2θ of 26.63°, 33.73°,37.94°, and 51.79° can be indexed as the (1 1 0), (1 0 1), (2 0 0), and (2 1 1) planes of tetragonal rutile structure of stannic oxide (lattice constant a = 4.7373(2) Å et b = 3.1865(3) Å), which is in good agreement with standard value (JCPDS file No. 41–1445). The crystallite sizes of pure SnO_2, d_{XRD}, deduced from the XRD patterns by calculation of the Scherrer equation, was found to be 50 nm. The diffraction peaks of the $Cubi_2O_4$ precursor (Fig. 1b) at 2θ of 28.03°, 29.73°, 30.73°, 32.54°, 33.36° and 46.71° were respectively indexed as (2 1 1), (2 2 0), (0 0 2), (1 0 2), (3 1 0), and (4 1 1) planes of pure tetragonal phase of crystalline $Cubi_2O_4$, according to the Joint Committee Powder Diffraction Standards ($P4_2/mnm$, JCPDS file No. 42–0334) with lattice constants (a = 8.5004 Å, c = 5.819 Å) calculated from their corresponding XRD pattern data obtained by Fullprof program. Both precursors $CuBi_2O_4$ and pure SnO_2 show preferred (0 0 2) crystallographic orientation owing to the preparation route of the sample during the XRD analysis. On the other hand, the XRD patterns of (5 wt%) $CuBi_2O_4/SnO_2$ nanocomposite exhibited characteristic diffraction peaks of both $CuBi_2O_4$ and SnO_2 crystalline phases, suggesting that $CuBi_2O_4$ and SnO_2 are coexistent in the composites as separate phases. It can be seen from Fig. 1c, that at 5% mass concentration of $Cubi_2O_4$, the diffraction pattern of the nanocomposite materials was approximately similar to that of pure SnO_2. This is probably due to the high crystallinity of the SnO_2 phase and the lowest amount of $CuBi_2O_4$ present in the composites (5 wt%), thus appearing as the dominant peaks in the XRD spectra of the nanocomposite sample. Compared with SnO_2, the XRD patterns (Fig. 2) in the 2θ range from 20° to 37° of (5 wt%) $CuBi_2O_4/SnO_2$ exhibits the same broader peaks, indicating a high solubility of $CuBi_2O_4$ in SnO_2 matrix. Thus the presence of (5 wt%) $Cubi_2O_4$ has obviously no effect on the particle size of the (5 wt%) $CuBi_2O_4/SnO_2$ nanocomposite.

3.2. SEM analysis

Fig. 3a, illustrates typical SEM image of $CuBi_2O_4$ powder synthesized by solid-state reaction of CuO and α-Bi_2O_3 at 750 °C for 24 h, pure SnO_2 and (5 wt%) $CuBi_2O_4/SnO_2$ nanocomposites. It can be seen that, for the $CuBi_2O_4$, the appearance is a shapeless sheet, and the particle size of the $CuBi_2O_4$ is about 10–20 μm. Fig. 3b shows typical high-resolution SEM image of $CuBi_2O_4$ powder to further show the details of the nanoparticles. As shown in Fig. 3b, it clearly shows two different crystal shapes on the $CuBi_2O_4$ surface, corresponding to two different particle sizes of $CuBi_2O_4$. The appearance of $CuBi_2O_4$

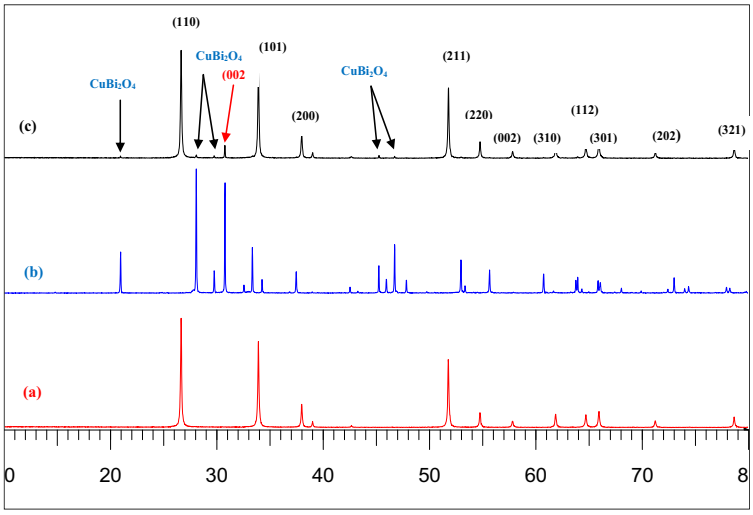

Figure 1 XRD patterns of pure SnO_2 (a) precursor $CuBi_2O_4$ (b) and the synthesized (5 wt%) $CuBi_2O_4/SnO_2$ (c).

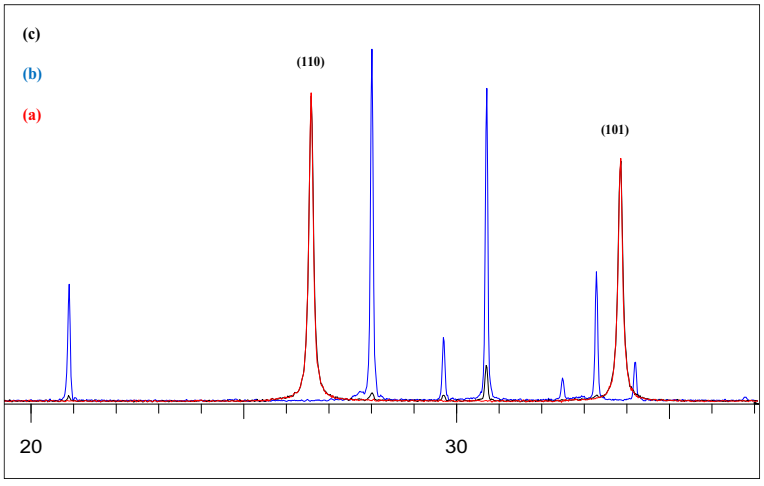

Figure 2 XRD patterns of pure SnO_2 (a) precursor $CuBi_2O_4$ (b) and the synthesized (5 wt%) $CuBi_2O_4/SnO_2$ (c) in the 2θ range from 20 to 37.

is a shape sheet and a well-defined tetragonal phase with the crystallite diameter of the $CuBi_2O_4$ about 5 μm, whereas groups of smaller particles do not have any specific shape with size up to 500 nm tend to cover the bigger particles. However, pure SnO_2 from SEM analysis (Fig. 3c) clearly shows two different tetragonal-shaped nanoparticle structures on the SnO_2 surface, which can be assigned to SnO_2 (ion radius Sn^{4+}: $rSn^{4+} = 0.071$ nm) with a particle size in the range of 0.1 μm and SnO (ion radius Sn^{2+}: $rSn^{2+} = 0.112$ nm) with approximately 0.2 μm dimensions, which agrees with the UV–Vis diffuse reflectance spectrum of SnO_2 in Fig. 4. Both nanoparticles are close to each other in the form of chains.

The as synthesized (5 wt%) $CuBi_2O_4/SnO_2$ nanocomposite via the physical milling synthesis method (Fig. 3d) clearly shows the presence of SnO_2 nanoparticles deposited onto the $CuBi_2O_4$ surface, displaying a particle size of 0.1–0.2 μm and strong assembly of the nanoparticles measuring from 0.2 μm to 1 μm. Such aggregation can be explained by the solid-state synthesis route, which generally requires repeated mechanical mixing process and a high temperature process.

3.3. UV–Vis diffuse reflectance spectra and band gap energy

Fig. 4, shows the UV–Vis absorbance spectra of $CuBi_2O_4$ synthesized by solid-state reaction at 750 °C for 24 h and pure SnO_2. It is clear from the recorded UV–visible spectrum of SnO_2 that two absorption bands are observed in the UV region at 210–245 nm and at 270 nm. Generally, the absorption band at 210–245 nm of SnO_2 in the UV region originates from the charge-transfer transition between the O 2p and Sn 4d states in O^{2-} and Sn^{4+}. The band at 270 nm is attributed, either to the inter-valence transition of Sn^{4+}/Sn^{2+} (Shen et al., 1994), or to the charge-transfer transition $s \rightarrow p$ of Sn^{2+} ions (Teegarden, 1966).

The UV–visible spectrum of $CuBi_2O_4$ nanostructures synthesized by solid-state reaction at 750 °C for 24 h is presented in Fig. 4. It can be seen that it has strong and broad absorption in the range of 200–900 nm. This suggests that the prepared sample absorbs both UV and visible light. Obviously, for $CuBi_2O_4$ nanostructures, the broad absorption band observed in the UV–visible region was attributed to the charge-transfer

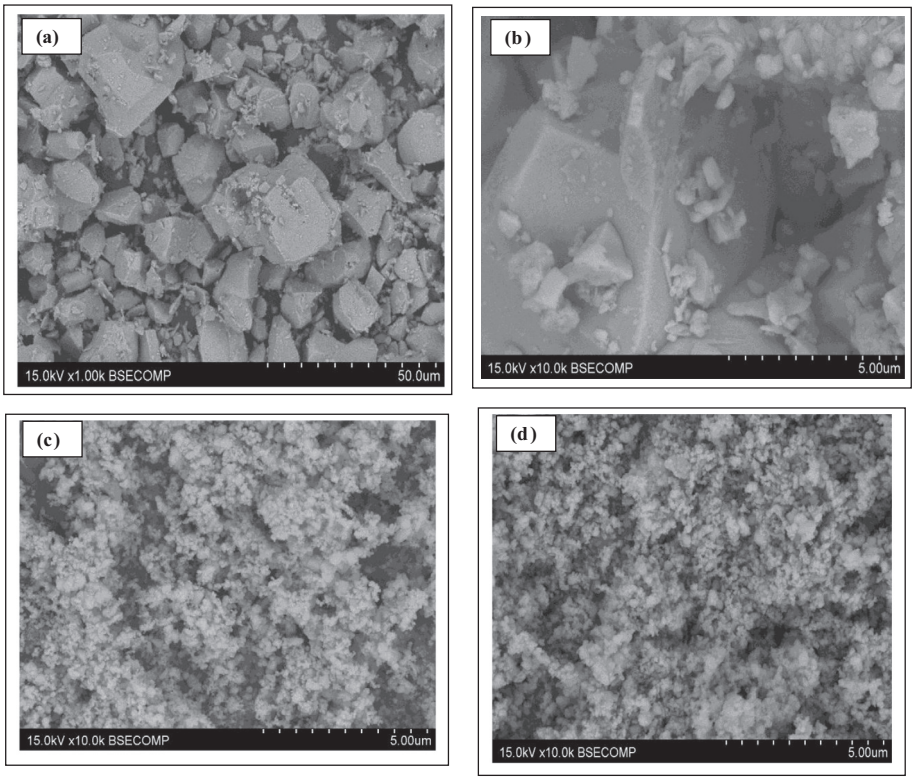

Figure 3 SEM images of (a) low-resolution of $CuBi_2O_4$ (b) high-resolution of precursor $CuBi_2O_4$ (c) pure SnO_2 (d) (5 wt%) $CuBi_2O_4/SnO_2$ nanocomposites.

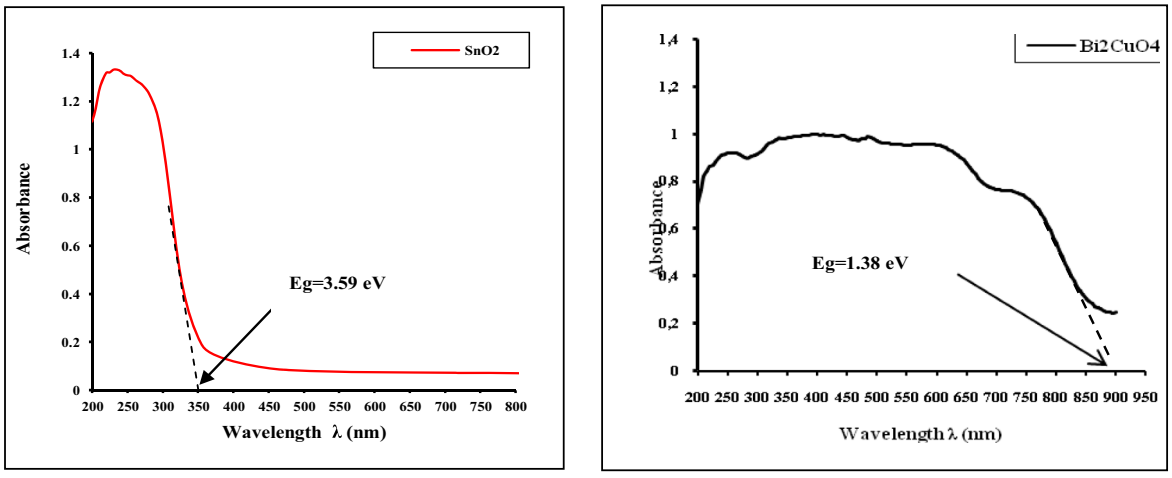

Figure 4 UV–visible absorbance spectra of SnO_2 and $CuBi_2O_4$ synthesized by solid-state reaction at 750 °C for 24 h.

transition between the O 2p and Cu $3dx^2 - y^2$ states in O^{2-} and Cu^{2+}, respectively (Nathan et al., 2012). Fig. 5 shows UV–Vis diffuse reflectance spectra of a series of photocatalysts (x wt%) $CuBi_2O_4/SnO_2$ for x = 0–20 wt%. A progressive red shift in the band gap absorption is observed with an increase in the amount of (x wt%) $CuBi_2O_4$ in the SnO_2 matrix.

Pure SnO_2 has a negligible absorption in the range of UVA light (355 nm $\leqslant \lambda \leqslant$ 375 nm) because the catalyst is only effective under ultraviolet irradiation ($\lambda \leqslant$ 345 nm). With an increase in the amount of x wt% of $CuBi_2O_4$, the absorption edge of the sample has some red shift. The red-shift observed in the nanocrystalline SnO_2 would explain the formation of localized states within the band gap owing to oxygen vacancies and increase in Sn^{2+} ion concentration. This phenomenon is due to the shift of absorbance band toward the longer wavelength (Lu et al., 2009; Charitidis et al., 2005). The red shift is presumably ascribed to the homogeneous dispersion of $CuBi_2O_4$ particles within SnO_2 matrix. The onset absorption edges and band gap energies of the as-synthesized $CuBi_2O_4$ particle, pure SnO_2 nanoparticle and series of (x wt%)

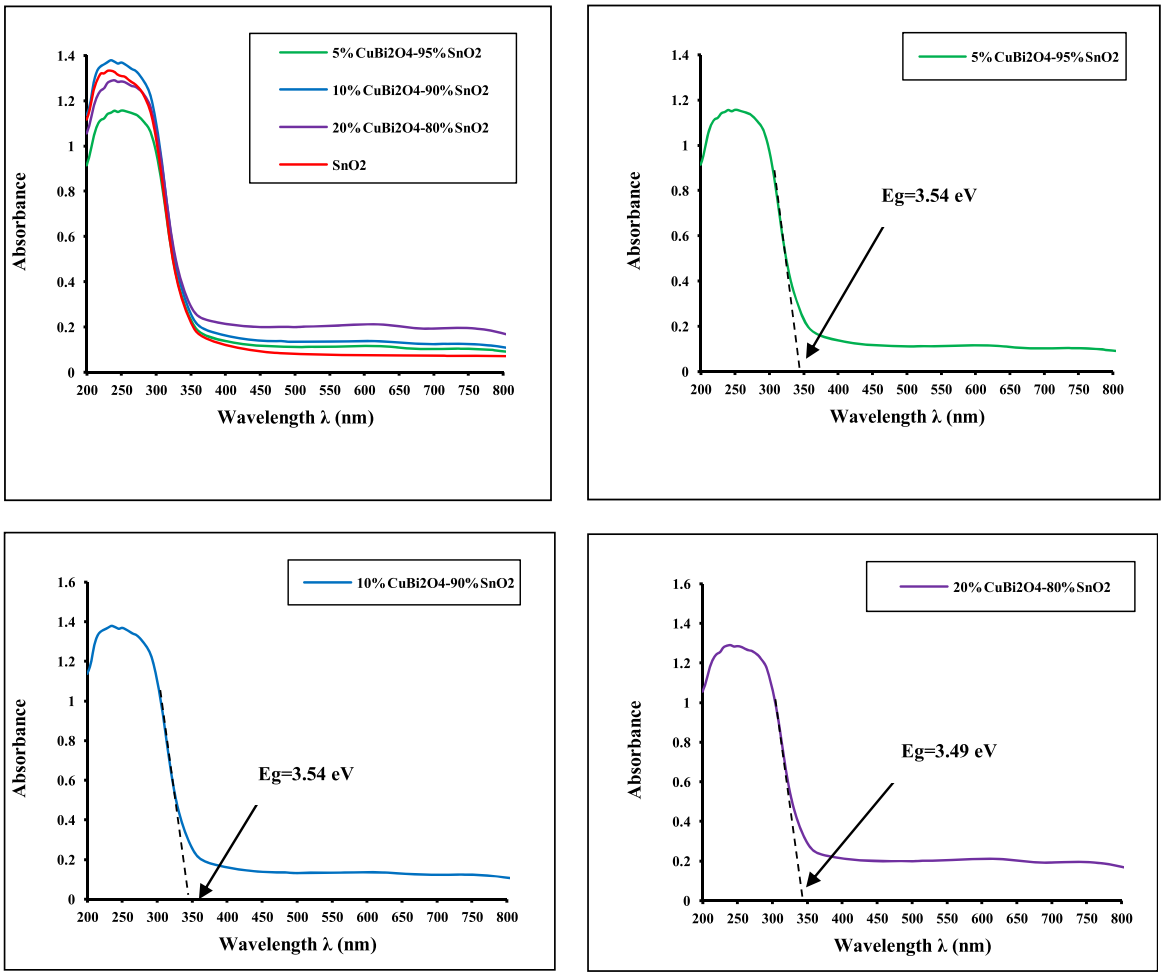

Figure 5 UV–visible absorbance spectra of a series of (x wt%) $CuBi_2O_4/SnO_2$ (with x = 0–20 wt%) nanocomposites.

Table 1 Optical properties of the as-synthesized $CuBi_2O_4$ and pure SnO_2 nanoparticles.

Systems	λ (nm)	Charge-transfer transition	Band gap Eg (eV)	
			Experimental	Literature Refs.
$CuBi_2O_4$	900	$2p^6(O) \rightarrow 3dx^2\text{-}y^2$ (Cu)	1.38	1.5 (Arai et al., 2007; Liu et al., 2010a,b)
SnO_2	345	$2p^6$ (O) → 5*s* (Sn)	3 .59	3.5–4.1 (Casey and Stephenson, 1990)
05	350	$2p^6$ (O) → 5*s* (Sn)	3.54	
10	350	$2p^6$ (O) → 5*s* (Sn)	3.54	
20	355	$2p^6$ (O) → 5*s* (Sn)	3.49	

λ: Wavelength, Refs.: References.

$CuBi_2O_4/SnO_2$ nanocomposites are shown in Figs. 4 and 5, respectively.

The absorption onsets of crystalline semiconductor were determined by linear extrapolation from the infection point of the curve (Absorbance versus $\lambda_{Absorp.\ Edge}$) to the baseline and Eg = $1240/\lambda_{Absorp.\ Edge}$ as shown in Figs. 4 and 5. The as-synthesized $CuBi_2O_4$ exhibits an absorption onset at 900 nm, which corresponds to the band gap energy of 1.38 eV. This value is lower than that reported in the literature; 1.5 eV (Arai et al., 2007; Liu et al., 2010a,b). It is clear from the recorded spectrum (Fig. 4) that the pure nanocrystalline SnO_2 has an absorption onset at 345 nm, which matches the band gap energy of 3.59 eV, attributing to stannic oxide (SnO_2). These results are well in agreement with values reported in the literature (Casey and Stephenson, 1990). The optical properties of the as-synthesized $CuBi_2O_4$ and pure SnO_2 nanoparticles are reported in Table 1.

It is widely accepted that electronic transport properties depend on the physical and structural characteristics of photocatalyst, such as crystallite size, morphology, phase structure and amount of $CuBi_2O_4$ loaded (Yu et al., 2008). As reported from the UV–visible results in Fig. 5 and Table 1, for the series of (x wt%) $CuBi_2O_4/SnO_2$ nanocomposite materials, the band gap energy slightly decreased from 3.59 to 3.49 eV as the

amount of $CuBi_2O_4$ was increased up to 20 wt% on the SnO_2 matrix, suggesting that a number of micro p–n heterostructures $CuBi_2O_4/SnO_2$ will be formed after doping $CuBi_2O_4$ powder into SnO_2 particles. Hence it was concluded that $CuBi_2O_4$ played a role in electron separation. The increase in photocatalytic activity of $CuBi_2O_4/SnO_2$ would be attributed to the suppression of electron–hole recombination by the effective electron separation (Masami et al., 2013). So, the decrease in the band gap energy with an enhanced absorption intensity of the (5wt%) $CuBi_2O_4/SnO_2$ nanocomposites upon loading the amount of $CuBi_2O_4$ could be ascribed to the homogeneous dispersion of $CuBi_2O_4$ within the SnO_2 matrix in the bulk of the catalyst and the formation of conducting network at very low temperature.

Chun-Ming et al. (2007) have already reported band gap narrowing effect for doped SnO_2 nanoparticles. However there is no clear understanding of this phenomenon. A direct–indirect transition has been proposed by Rakhshani et al. (1998). In order to explain the band gap narrowing effect, many groups have suggested that alloying effect of parent compound with some impurity phases may be responsible for the band gap narrowing (Park and Kim, 2003; Barreau et al., 2002). So we think that for the samples containing up to 5 wt% $CuBi_2O_4$ concentration, SnO_2–SnO_{2-x} alloying effect may be responsible for the band gap narrowing effect. For the SnO_2 nanoparticles above 5 wt% $CuBi_2O_4$ concentration there is a huge drop in the band gap. This may be due to the formation of sub-bands in between the band gap and the conduction band and sub-bands are merging with the conduction band to form a continuous band. This is perfectly in agreement with the XRD analytical results and consistent with the previously reported work (Chun-Ming et al., 2007).

3.4. Photocatalytic activity tests

3.4.1. Effect of pH solution on the photocatalytic activity of (5 wt%) $CuBi_2O_4/SnO_2$ nanocomposite

In order to study the effect of initial pH on the degradation efficiency of (5 wt%) $CuBi_2O_4/SnO_2$ nanocomposite catalyst on photodecomposition of CR, experiments were carried out at various pH, ranging from 6 to12 for avoiding dye aggregation. Results showed that the pH significantly affected the photocatalytic degradation efficiency of both CR. As shown in Fig. 6 and Table 2, for CR, the degradation rate increased from 12.03 to 58.06% as the pH value was increased from 6 to 8, and then decreased to 12.27 at pH 12. The maximum degradation rate of CR (58.06%) was achieved at pH 8. For this reason, the pH 8 was selected for subsequent experiments.

Table 2 Results of the effect of the pH solution on the photocatalytic redox of CR under UVA light irradiation ([(5 wt% $CuBi_2O_4/SnO_2$] = 0.5 g/L, [CR] = 20 mg/L, T = 298 K, λ_{max} = 365 nm, I = 90 J/cm^2 and irradiation time = 100 min).

pH initial	Adsorption activity η (%)	Photocatalytic activity η′ (%)
2	Dye aggregation	
4		
6	0.93	12.03
7	33.69	42.16
8	31.38	58.06
10	8.64	13.77
12	0.46	12.27

It is commonly accepted that in photocatalyst/aqueous systems, the potential of the surface charge is determined by the activity of ions (e.g. H^+ or pH). A convenient index of the tendency of a surface to become either positively or negatively charged as a function of pH is the value of the pH required to give zero net charge (pH_{PZC}) (Zhang et al., 1998; Yath, 1974). pH_{PZC} is a critical value for determining the sign and magnitude of the net charge carried on the photocatalyst surface during adsorption and the photocatalytic degradation process. Most of the semiconductor oxides are amphoteric in nature, can associate Eq. (15) or dissociate Eq. (17) proton. To explain the relationship between the layer charge density and the adsorption, so-called Model of Surface Complexation (SCM) was developed (Fernandez et al., 2002), which consequently affects the sorption–desorption processes as well as the separation and transfer of the photogenerated electron–hole pairs at the surface of the semiconductor particles. In the 2-pK approach we assume two reactions for surface protonation.

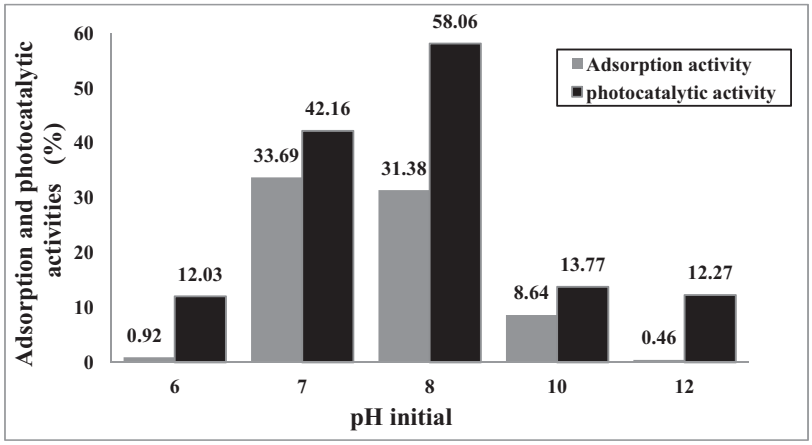

Figure 6 Effect of the pH solution on the photocatalytic redox of CR under UVA light irradiation ([(5 wt% $CuBi_2O_4/SnO_2$] = 0.5 g/L, [CR] = 20 mg/L, T = 298 K, λ_{max} = 365 nm, I = 90 J/cm^2 and irradiation time = 100 min).

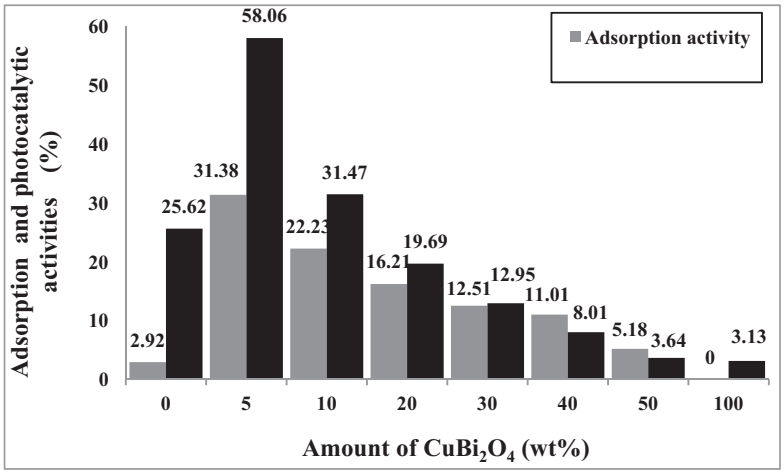

Figure 7 Effect of the amount of $CuBi_2O_4$ on the photocatalytic redox of CR under UVA light irradiation ([(x wt%) $CuBi_2O_4$/SnO_2] = 0.5 g/L, [CR] = 20 mg/L, pH = 8, T = 298 K, λ_{max} = 365 nm, I = 90 J/cm^2 and irradiation time = 100 min).

The zero point charge pH $_{PZC}$ for SnO_2 (about 5) is approximately identical to that of (5 wt%) $CuBi_2O_4/SnO_2$ which is mainly composed of SnO_2 nanopowders (shown in XRD patterns), since there is no adsorption of CR ions than the potential determining H^+/OH^- at the surface of $CuBi_2O_4$ particles. This is often the case for pure (''pristine surface'') oxides in water.

When the pH is lower than the pH $_{PZC}$ value, the system is said to be ''below the PZC''. Below the PZC, the acidic water donates more protons than hydroxide groups, and so the adsorbent surface is positively charged (attracting anions/repelling cations), according to the following reaction Eqs. (9), (10):

$$\mathrm{pH} < \mathrm{pH}_{PZC}$$
$$(5\,\mathrm{wt\%})\ CuBi_2O_4SnO_2 + H^+ \rightarrow (5\,\mathrm{wt\%})\ CuBi_2O_4SnO_2H^+ \quad (9)$$

$$(5\,\mathrm{wt\%})\ CuBi_2O4/SnO_2H^+ + CR^- \rightarrow [(5\,\mathrm{wt\%})\ CuBi_2O_4/SnO_2H^+, CR^-]\ \text{(electrostatic interaction)} \quad (10)$$

Conversely, above pH $_{PZC}$ the surface is negatively charged (attracting cations/repelling anions), given by the following reaction Eqs. (11) and (12):

$$\mathrm{pH} > \mathrm{pH}_{PZC}\quad (5\,\mathrm{wt\%})\ CuBi_2O_4/SnO_2 + OH^- \rightarrow (5\,\mathrm{wt\%})\ CuBi_2O_4/SnO^- + H_2O \quad (11)$$

$$(5\,\mathrm{wt\%})\ CuBi_2O_4/SnO^- + CR^- \rightarrow [(5\,\mathrm{wt\%})\ CuBi_2O_4/SnO^-, CR^-]\ \text{(electrostatic repulsion)} \quad (12)$$

The experimental data revealed that higher adsorption and degradation activities of CR were obtained in alkali medium (i.e. pH = 8). Even though (5 wt%) $CuBi_2O_4/SnO_2$ nanocomposite showed good photocatalytic efficiency among the $CuBi_2O_4$ loadings, but it seems to be that this activity may not be up to our expectation. The poor adsorption affinity of the composite toward organic pollutant may be the primary cause of the observed efficiency. As the adsorption reaction between anionic dye/composite takes place on the solid surface, this means that the main dye-composite interaction is a coulomb-type interaction. However, other interaction, such as hydrophobic effect between guest molecules on the composite surface (Xie et al., 2005) and/or H-bonding can contribute to the adsorption of organic dye on composite surface, favoring the dye agglomeration. Thus, the enhancement of adsorption activity was not exclusively caused by the attractive interaction among dye-composite because there are no obvious electrostatic interactions between the negatively charged (5wt%) $CuBi_2O_4/SnO_2$ surface (pH > pH $_{PZC}$) and CR anionic dye (pH > pK_a) at pH 8. As was reported previously, we believe that it is mainly due to the hydrophobic effect between guest molecules on the composite surface and/or H-bonding. Thus, a strong adsorption can lead to a drastic decrease in the active centers on the catalyst surface, which results in a decrease in the absorption of the light quanta by the catalyst and consequently reducing the kinetic reaction. As a result, the moderate photodegradation activity can be ascribed to the (5 wt%) $CuBi_2O_4/SnO_2$-mediated photocatalytic oxidation of CR dye under alkali medium. It is noteworthy that heterogeneous photocatalytic processes substantially depend on a variety of environment conditions as mentioned in Introduction section. Thus, the presence of the tightly physically bonded or close contact interfaces between

Table 3 Results of the effect of the amount of $CuBi_2O_4$ on the photocatalytic redox of CR under UVA light irradiation ([(x wt%) $CuBi_2O_4/SnO_2$,0.5 g/L, [CR] = 20 mg/L, pH = 8, T = 298 K, λ_{max} = 365 nm, I = 90 J/cm^2 and irradiation time = 100 min).

Amount of $CuBi_2O_4$ x (%)	Adsorption activity η (%)	Photocatalytic activity η′ (%)
0	2.92	25.62
5	31.38	58.06
10	22.24	31.48
20	16.21	19.69
30	12.52	12.95
40	11.01	8.01
50	5.18	3.64
100	4.71	3.13

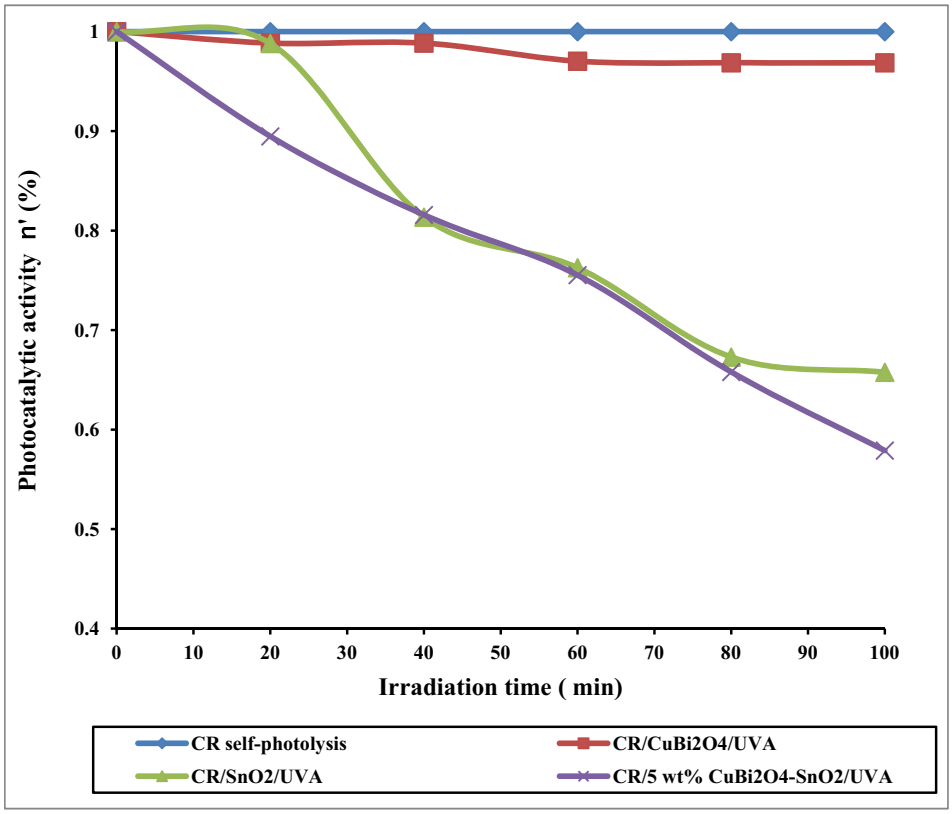

Figure 8 Photocatalytic degradation kinetics of CR at different experimental conditions ([Catalyst] = 0.5 g/L, [CR] = 20 mg/L, pH = 8, T = 298 K, λ_{max} = 365 nm, I = 90 J/cm^2 and irradiation time = 100 min).

the two materials, by which the photoinduced charge transfer from one particle to the other through interfaces spatially is available, can lead to a strong photocatalytic redox of CR over the combined catalysts.

At neutral and acidic media (pH < 8), lower photocatalytic efficiency of catalyst can be explained by the following possible reasons. First, the electrostatic repulsion forces between the negatively charged (5 wt%) $CuBi_2O_4/SnO_2$ surface and CR anionic dye, mainly sulfonated groups ($-SO_3^-$), affecting strongly the accessibility of the surface reducing species to the CR photocatalytic oxidation/reduction kinetics. Second, the excess of H_3O^+ ions, especially at pH = 6, enters into electrostatic interactions with both the negatively charged (5 wt%) $CuBi_2O_4/SnO_2$ surface and RC dye anions, leading to a minimum adsorption extent at pH 6. Furthermore we found that, where the adsorption of dye was strong, photodegradation remarkably occurred.

At pH higher than pH_{PZC} value (i.e. pH > 8), excess of hydroxyl anions facilitates photogeneration of $^{\bullet}OH$ radicals which are accepted as primary oxidizing species responsible for photocatalytic degradation, resulting in the enhancement of the efficiency of the process. However, a dramatic decrease in the degradation efficiency could be explained on the basis of amphoteric behaviors of (5 wt%) $CuBi_2O_4/SnO_2$ catalyst. The negatively charged surface of (5 wt%) $CuBi_2O_4/SnO_2$ catalyst (highly concentration of hydroxide ions) and the great negatively charged RC dye anions resulted in electrostatic repulsion, leading to the reduction in the efficiency of the photodegradation process. There were similar results in the previous reports (Liu et al., 2010a,b).

3.4.2. Effect of the amount of $CuBi_2O_4$ on the photocatalytic activity of (x wt%) $CuBi_2O_4/SnO_2$

The effect of the amount of $CuBi_2O_4$ on photocatalytic degradation of CR was conducted over a range of catalyst amounts from x = 0 to x = 100 wt%. As observed in Fig. 7 and Table 3, it is evident that the photocatalytic redox of CR greatly depends on the amount of doped $CuBi_2O_4$. The photocatalytic activity increased drastically from 25.62 to 58.06% as the catalyst amount was raised from x = 0 to x = 5 wt%. Upon further increase in the $CuBi_2O_4$ amount beyond x = 5 wt%, the photocatalytic activity decreased gradually, almost reaching 3.13% at x = 100 wt%. The maximum photocatalytic activity of (x wt%) $CuBi_2O_4/SnO_2$ (58.06%) under UVA light irradiation was achieved within 100 min of light illumination time when the amount of doped $CuBi_2O_4$ x was 5 wt%, which is obviously about 2.3 times higher than the value of 25.62% over pure SnO_2. So there is an optimum $CuBi_2O_4$ contents for high dispersion morphology of nanoparticles $CuBi_2O_4$ on the SnO_2 surface with high activity. The effective electron–hole separation both at the physically bonded interfaces and in the two semiconductors as well as charge defect during the physical mixing method was believed to be mainly responsible for the remarkably enhanced photocatalytic activity of (5 wt%) $CuBi_2O_4/SnO_2$ in the course of the photocatalytic redox conversion of CR. But until now,

Table 4 Kinetic parameters of photocatalytic degradation of CR on (5 wt%) $CuBi_2O_4/SnO_2$, compared to the pure and combined catalyst systems ([Catalyst] = 0.5 g/L, [CR] = 20 mg/L, pH = 8, T = 298 K, λ_{max} = 365 nm, I = 90 J/cm^2 and irradiation time = 100 min).

Systems	Adsorption activity η (%)	Photocatalytic activity η′ (%)	K_1 (min^{-1})	$t_{1/2}$ (min)	R^2 (%)
CR/UV-A	–	0.49	–	–	–
CR/SnO_2/UVA	2.92	25.62	0.0045	154.032	0.945
CR/$CuBi_2O_4$/UVA	0	3.130	0.0002	3465.736	0.203
CR/(5 wt.%)$CuBi_2O_4$-SnO_2/UVA	31.38	58.06	0.052	13.329	0.991

Table 5 Absolute electronegativity, estimated band gap, energy levels of calculated conduction band edge, and valence band at the point of zero charge for p-$CuBi_2O_4$ and n-SnO_2.

Systems	χ (eV)	λ (nm)	Eg (eV)	E^0_{BC} (eV)	E^0_{BV} (eV)
p-$CuBi_2O_4$	4.75	900	1.38	−0.44	+0.94
n-SnO_2	6.25	345	3.59	−0.05	+3.55

there are no reports about synergistic effect between SnO_2 and $CuBi_2O_4$ in the (5 wt%) $CuBi_2O_4/SnO_2$ nanocomposite under visible light excitation. From Fig. 7, it is clear that the photocatalytic activity of SnO_2 is significantly increased under the presence of an amount of $CuBi_2O_4$ (5 wt%) compared to pure SnO_2 and the $CuBi_2O_4$ samples. These results strongly suggest the existence of a synergistic effect between SnO_2 and the $CuBi_2O_4$ in the (5 wt%) $CuBi_2O_4/SnO_2$ nanocomposite under UVA light excitation.

However, at higher amount of doped $CuBi_2O_4$ than 5 wt%, the photocatalytic redox activity of (x wt%) $CuBi_2O_4/SnO_2$ photocatalyst was obviously decreased on further increase in the amount of $CuBi_2O_4$. Thus, such an above occurrence in the present experiment is primarily attributed to overlapping of adsorption sites of SnO_2 particles as a result of overcrowding of the $CuBi_2O_4$ granule owing to the decrease in screening effect and interfering of light. Similar trends were reported in a series of p–n heterojunction photocatalysts p-$CuBi_2O_4$/n-TiO_2 (Lin et al., 2008) and $CuBi_2O_4$/$BiVO_4$ (Masami et al., 2013) with high photocatalytic activity under visible and UV light irradiation.

3.4.3. Effect of UV light and catalyst

The photocatalytic activities of all three $CuBi_2O_4$, SnO_2 and (5 wt%) $CuBi_2O_4/SnO_2$ photocatalysts were assessed by the photocatalytic redox reaction of Congo red (CR) aqueous solution under UVA light irradiation. Variations of CR reduced concentration (C/C_0) versus visible-light irradiation time over different catalysts under different experimental conditions through alone (CR self-photolysis), $CuBi_2O_4$/UVA, SnO_2/UVA and (5 wt%) $CuBi_2O_4/SnO_2$/UVA are presented in Fig. 8. The synergistic effect between SnO_2 and $CuBi_2O_4$ in the (5 wt%) $CuBi_2O_4/SnO_2$ nanocomposite under UVA light excitation showed that (5 wt%) $CuBi_2O_4/SnO_2$ exhibited

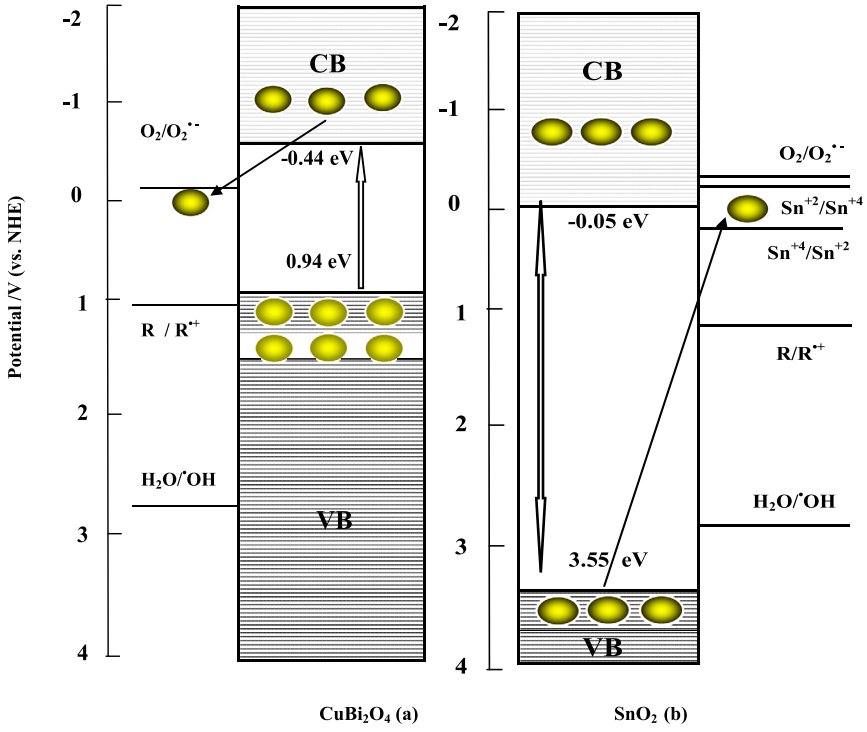

Figure 9 Reaction schemes of $CuBi_2O_4$ (a) and SnO_2 (b) as the p- and n-type semi-conductor respectively for charge separation for the reductivity/oxidizability improvement model (electron and hole).

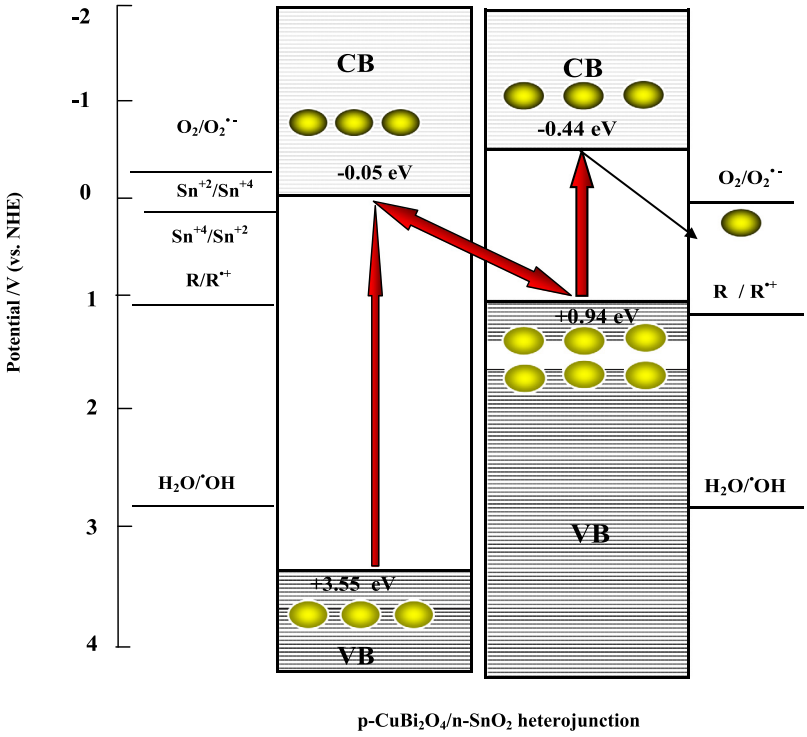

Figure 10 Mechanism of CR degradation in a z-scheme photocatalysis system consisting of $CuBi_2O_4/SnO_2$ heterojunction under UVA-light irradiation. (electron and hole).

higher photocatalytic efficiency, as compared to the single phases $CuBi_2O_4$ and SnO_2. The highest efficiency was obtained, under UVA light irradiation over (5 wt%) $CuBi_2O_4/SnO_2$, as a result of 58.06% degradation of CR for 100 min of irradiation time. However, the photocatalytic degradation of CR over single phases $CuBi_2O_4$ and SnO_2 was only 3.13 and 25.62% respectively. With 20 mg/L of CR in the direct photolysis for the same optimum irradiation time, disappearance of dye was negligible (0.49%). On the basis of these results, the high decomposition of CR dye in the presence of (5 wt%) $CuBi_2O_4/SnO_2$ catalyst is exclusively attributed to the photocatalytic reaction of the combined semiconductor particles under UVA light irradiation. As known, one of the basic requirements for the combined photocatalysts with a higher activity is the presence of the tightly physically bonded or close contact interfaces between the two materials, by which the photoinduced charge transfer from one particle to the other via interfaces spatially is available. Thus, such an above occurrence in the present experiment is primarily assigned to the charge defect during the physical mixing method, which is advantageous for the effective electron–hole separation and the suppression of the recombination rate of the photogenerated charge carriers; hence result in an improvement of the probability of light-generated carriers transfer via interfaces spatially available. A similar result was reported in the heterojunction semiconductor $SnO_2/SrNb_2O_6$ with an enhanced photocatalytic activity (Gurlo, 2006).

3.4.3.1. Kinetic modeling. The photocatalytic degradation of CR over different experimental conditions is displayed in Table 4. As it can be seen, the straight lines for the entire as-prepared samples of the plots of ln C/C_0 versus t with high regression coefficients (R^2 = 0.945–0.991), for the pseudo-first-order kinetic model strongly suggest that all the photodegradation systems were a pseudo-first-order model. Exception was observed in the cases of direct photolysis and photocatalysis reaction in the presence of the single phase $CuBi_2O_4$ respectively.

3.5. Discussion of mechanism

The above analysis shows that the migration direction of the photogenerated charge carrier depends on the band edge positions of the two semiconductors. There are three methods to determine the band edge positions: experiments based on photoelectrochemical techniques, calculation according to the first principle, and predicting theoretically from the absolute (or Mulliken) electronegativity (Kim et al., 1993; Butler and Ginley, 1978; Xu and Schoonen, 2000). The first one is not always easy to handle, and the second one cannot obtain the absolute energy of band edges with respect to vacuum and always has large discrepancies between calculated and measured values. The third one is a simple approach with reasonable results for many oxide photocatalysts (Xu and Schoonen, 2000). The conduction band edge of a semiconductor at the point of zero charge (pHzpc) can be predicted by Eq. (13):

$$E^0_{CB} = \chi - E_C - 1/2Eg. \quad (13)$$

where χ is the absolute electronegativity of the semiconductor (χ is 4.75 eV and 6.25 eV for p-$CuBi_2O_4$ and n-SnO_2, respectively). EC is the energy of free electrons on the hydrogen scale

(4.5 eV) and Eg is the band gap of the semiconductor. The predicted band edge positions of $CuBi_2O_4$ and SnO_2 by the above equation are shown in Table 5. Photocatalytic reaction proceeds owing to holes and electrons generated in materials by absorbing light energy. The photogenerated holes have oxidation ability and the photogenerated electrons have reduction ability. For decomposition of organic pollutants by photocatalytic reaction, the oxidation potential of hole needs to be more positive than + 1 V that is redox potential of general organic compounds as well as of hydroxyl radical (E_0 ($H_2O/^{\bullet}OH$)) = 2.8 V/NHE at pH 7). In addition, the redox potential of electrons needs to be more negative than that of superoxide radical (E_0 ($O_2/O_2^{\bullet-}$) = -0.28 V/NHE at pH 7).

Fig. 9 depicts reaction schemes of $CuBi_2O_4$ (a) and SnO_2 (b) as the p and n type respectively for charge separation for the reductivity/oxidizability improvement model. $CuBi_2O_4$ is a p-type semiconductor, which always exhibits good stability under UVA visible illumination, and SnO_2 is determined as an n-type material. It was reported previously that that the band gap of $CuBi_2O_4$ is 1.38 eV, which can be excited by photons with wavelengths below 900 nm, whereas SnO_2 with band gap of about 3.59 eV can be excited by photons with wavelengths of 345 nm. Under UVA (λ_{UVA} = 355–375 nm → Eg_ = 3.3–3.49 eV) light irradiation, the energy of the excitation light is sufficient to directly excite the $CuBi_2O_4$ (λ = 900 nm → Eg = 1.38 eV) semiconductor and it is large enough to yield a higher energy level of SnO_2 (λ = 345 nm → Eg = 3.59 eV) portion of the photocatalyst.

According to the band edge position (Table 5), for the p-$CuBi_2O_4$ alone (Fig. 9 a), the electronic potential of the conduction band of p-$CuBi_2O_4$ is around −0.44 eV/NHE at pH 7 which is more negative than that of superoxide radical (E_0 ($O_2/O_2^{\bullet-}$) = −0.28 V/NHE at pH 7). This indicated that the electron photoproduced at the conduction band directly reduced O_2 into $O_2^{\bullet-}$. These reduced $O_2^{\bullet-}$ can subsequently transfer the charge to the species present in the reaction medium that is preferentially adsorbed onto the p-$CuBi_2O_4$ particles. Hence, the superoxide radical ($O_2^{\bullet-}$) reduces the recombination of the charge carriers enhancing the activity in the UVA light. However, the p-$CuBi_2O_4$ valence band of + 0.94 eV/NHE at pH 7, is too negative than that of hydroxyl radical (E_0 ($H_2O/^{\bullet}OH$)) = + 2.8 V/NHE at pH 7). The holes photogenerated in the p-$CuBi_2O_4$ are not able to oxidize H_2O to $^{\bullet}OH$.

p-$CuBi_2O_4$ powder formed in our laboratory by the solid-state reaction of CuO and α-Bi_2O_3 at 750 °C for 24 h, exhibits a black color. The presence of non stoichiometric regions of the nominally p-CuBi2O4 particles or small domains of binary oxide phases of Cu_xO or Bi_xO, undetected by XRD data, as unstable impurity phases which could be originated from a number of processes such as reduction of the p-$CuBi_2O_4$, could be responsible for higher recombination rates. Thus, the result is consistent with the previous study in the electrochemical synthesis and characterization of p-$CuBi_2O_4$ thin film photocathodes (Magesh et al., 2009). Therefore, $CuBi_2O_4$ alone shows negligible photocatalytic activity under UVA light. As a result, less efficient charge-carrier separation, and thus the increment of photocatalytic activity were restricted (Elaziouti et al., 2012).

For pure n-SnO_2 (Fig. 9b) which is only effective under ultraviolet irradiation (λ = 345 nm), shows little photocatalytic activity under UVA light. These observations can be explained as follows: The reduction of Sn^{+4} to Sn^{+2} requires a potential of + 0.15 V/NHE at pH 7 and the oxidation of Sn^{+2} to Sn^{+4} needs −0.15 V/NHE at pH 7. The SnO_2 valence band of SnO_2 is around + 3.55 eV (vs. NHE at pH 7) which is more positive than Sn^{+2} to Sn^{+4} oxidation potential. The valence electron of SnO_2 can hence oxidize Sn^{+2} to Sn^{+4}. But the conduction band of SnO_2 has a potential of −0.05 eV/NHE at pH 7, which is more negative than Sn^{+4} to Sn^{+2} reduction potential. Hence, the conduction band electrons of SnO_2 may be able to reduce Sn^{+4} to Sn^{+2}. These reduced Sn^{+2} and oxidized Sn^{+4} species can subsequently transfer the charge to the species present in the reaction medium. Hence, the Sn ions can suppress the recombination of the charge carriers, enhancing the activity in the UVA light.

In contrast, (5 wt%) p-$CuBi_2O_4$/n-SnO_2 composite exhibits a higher photocatalytic activity compared to that of single photocatalyst (p-$CuBi_2O_4$ and n-SnO_2). To overcome the recombination problem of composite photocatalyst while maintaining its high efficiency, an artificial z-scheme photocatalytic system, which mimics the z-scheme in the natural photosynthesis of green plants (Sasaki et al., 2008) has been suggested for p-$CuBi_2O_4$/n-SnO_2 composite mediated photocatalytic degradation of Congo red as probe pollutant. The solid state z-scheme mechanism, in which two UVA light sensitive photocatalysts, p-$CuBi_2O_4$ and n-SnO_2 in our case, with different levels of band gap energy Eg, is utilized without any intermediates. This system, however, cannot be considered to be a genuine z-scheme under irradiation by visible light because bare n-SnO_2, can only generate electrons when irradiated with UV light (Hyeong et al., 2011). The z-scheme photocatalysis system diagram is depicted in Fig. 10.

So, when p-type semiconductor $CuBi_2O_4$ and n-type semiconductor SnO_2 were connected to each other, a number of micro p–n heterojunction $CuBi_2O_4/SnO_2$ will be formed between p-$CuBi_2O_4$ powder and n-SnO_2 granule at the interfaces of p-$CuBi_2O_4$ loaded n-SnO_2 composite. According to the band edge position (Table 5), the electronic potential of the conduction band of n-SnO_2 is slightly more anodic than that of p-$CuBi_2O_4$, whereas, the hole potential of the valence band top of n- SnO_2, is more positive than that of p-$CuBi_2O_4$. The electron–hole pairs will be created under UVA light illumination. The electrons that are photogenerated by n-SnO_2 are transferred to the valence band of p-$CuBi_2O_4$. These electrons then recombine with holes photogenerated at p-$CuBi_2O_4$. The electrons that are excited at p-$CuBi_2O_4$ then have a sufficiently high potential to participate in the reduction step of the reaction. By taking advantage of a combination of p-$CuBi_2O_4$ and n-SnO_2, the probabilities of electron–hole recombination would be decreased significantly, thus resulting in more electrons available on $CuBi_2O_4$ surface and a larger amount of holes on SnO_2 surface acting as powerful oxidants respectively (Eqs. 14, 15). The stepwise photocatalytic mechanism is illustrated below:

$$\text{p-}CuBi_2O_4/\text{n-}SnO_2 + h\nu \rightarrow \text{p-}CuBi_2O_4(e^-_{BC} + h^+_{BV})/\text{n-}SnO_2(e^-_{BC} + h^+_{BV}) \quad (14)$$

$$\rightarrow \text{p-}CuBi_2O_4(e^-_{BC})/\text{n-}SnO_2(h^+_{BV}) \quad (15)$$

The electrons at the conduction band of p-$CuBi_2O_4$ react with the adsorbed molecular $O_{2ads.}$ on the p-$CuBi_2O_4$/n-SnO_2 catalyst sites, reducing it to superoxide anion ($O_{2\ ads}^{\bullet-}$),

hydroperoxide ($HO_{2\ ads}$) radicals and hydrogen peroxide ($H_2O_{2\ ads}$) (Eqs. (16)–(18)), while the holes at the valence electron of n-SnO_2 can directly oxidize the CR dye H_2O molecules adsorbed on the photocatalyst surface forming the organic cation-radicals ($R^{\cdot+}_{ads}$) (Eq. 20) and hydroxyl radicals ($^{\cdot}OH$) (Eq. 19). These processes could be represented in the following equations:

$$e^- + O_{2\ ads.} \rightarrow O^{\cdot-}_{2\ ads} \quad (16)$$

$$O^{\cdot-}_{2\ ads} + 2H_2O_{ads} \rightarrow HO^{\cdot}_{2ads} + OH_{ads} \quad (17)$$

$$HO^{\cdot}_{2ads} + H_2O_{ads} \rightarrow H_2O_{2ads} + {}^{\cdot}OH_{ads} \quad (18)$$

$$H_2O_{ads} + h^+ \rightarrow {}^{\cdot}OH_{ads} \quad (19)$$

$$R_{ads} + h^+ \rightarrow R^{\cdot}_{ads}{}^{+} \quad (20)$$

The peroxide (H_2O_{2ads}), hydroxylic ($^{\cdot}OH_{ads}$), hydroperoxide ($HO^{\cdot}_{2ads}$) and organic cation-radicals ($R^{\cdot+}_{ads}$) formed on the illuminated p-$CuBi_2O_4$/n-SnO_2 catalyst surface via z-scheme mechanism are highly effective oxidizing agent in the p-$CuBi_2O_4$/n-SnO_2 composite mediated photocatalytic oxidation of Congo red Eq. (21).

$$(H_2O_{2ads}, {}^{\cdot}OH_{ads}, O^{\cdot-}_{2ads}, R^{\cdot}_{ads}{}^{+}) + \text{CR dye} \rightarrow \text{degradation of the CR dye} \quad (21)$$

On the basis of the above results, photogenerated electron transfer between p-$CuBi_2O_4$ and n-SnO_2 photocatalysts is the rate-determining process in the solid state z-scheme photocatalytic system. Recently, Sasaki et al. had a surprising success in fabricating an overall water-splitting system driven by z-scheme interparticle electron transfer between H_2- and O_2-photocatalysts ($Ru/SrTiO_2$: $Rh\text{-}BiVO_4$) without a redox mediator (Sasaki et al., 2009; Iwase et al., 2011). Hyeong et al. reported on a novel strategy for generating H_2 fuel via an artificial photosynthesis system mimicking the z-scheme operation under visible light. They combined two visible sensitive photocatalysts, $TiO_{1.96}C_{0.04}$ and CdS which are used of this combination, that is, $CdS/Au/TiO_{1.96}C_{0.04}$. The system produced about a 4 times higher amount of H_2 under irradiation by visible light than $CdS/Au/TiO_2$ (Hyeong et al., 2013).

4. Conclusions

Novel p-$CuBi_2O_4$/n-SnO_2 nanocomposite photocatalysts with different mass ratios were synthesized with the solid state method, and were characterized by a number of techniques such as X-ray diffraction (XRD), scanning electron microscopy (SEM) and UV–Vis diffuse reflectance spectroscopy (DRS) technique. The as-prepared p-$CuBi_2O_4$/n-SnO_2 photocatalysts were assessed based on the photodegradation of Congo red (CR) dye as a probe reaction under UVA (365 nm) light irradiation. Experimental results indicated that the phase composition, surface morphology of particles, and optical absorption of the sample were found to vary significantly with the mass ratios and pH medium. The p-$CuBi_2O_4$/n-SnO_2 photocatalyst exhibited a higher photocatalytic redox activity than single phases $CuBi_2O_4$ and SnO_2. The photodegradation reactions were satisfactory correlated with the pseudo-first-order kinetic model. The highest efficiency was observed at 5 wt% p-$CuBi_2O_4$ content as a result of 58.06% of photoactivity for 100 min of exposure irradiation under UVA light at pH 8 and 25 °C. The effective electron–hole separation at the physically bonded interfaces was believed to be mainly responsible for the remarkably enhanced photocatalytic activity of 5 wt% $CuBi_2O_4/SnO_2$ in the course of the photocatalytic redox conversion of CR. The presence of the tightly physically bonded or close contact interfaces largely performed via hydrophobic effect between guest molecules on the composite surface and/or H-bonding by which the photoinduced charge transfer from one particle to the other through interfaces spatially is available, leading to a strong photocatalytic redox of CR at pH = 8. The efficient electron–hole separation process in z-scheme mechanism under UVA light irradiation was considered to be mainly responsible for the obviously improved photocatalytic activity of (5 wt%) $CuBi_2O_4/SnO_2$ catalyst in the course of the photocatalytic redox conversion of Congo red.

Acknowledgments

We are greatly indebted to the University of Science and Technology of Oran (Mohamed Boudiaf), and the University of Science and Technology of Saida (Moulay Tahar) for their material support. We gratefully acknowledge the support for X-ray diffraction (XRD), scanning electron microscopy (SEM) and UV–vis diffuse reflectance spectroscopy (DRS) by Mrs. Professor Rose-Noëlle Vannier of the Unit of Catalysis and Solid State Chemistry of Lille 1 University.

References

Aoki, A., Sasakura, H., 1970. Tin oxide thin film transistors. Jpn. J. Appl. Phys. 9, 582.

Arai, T., Yanagida, M., Konishi, Y., Iwasaki, Y., Sugihara, H., Sayama, K., 2007. Efficient complete oxidation of acetaldehyde into CO_2 over $CuBi_2O_4/WO_3$ composite photocatalyst under visible and UV light irradiation. J. Phys. Chem. C 111, 7574–7577.

Arham, S.A., Shafeeq, M.M., Singla, M.L., Sartaj, T., Naqvi, A.H., Azam, A., 2011. Band gap narrowing and fluorescence properties of nickel doped SnO_2 nanoparticles. J. Luminescence 131, 1–6.

Barreau, N., Bernede, J.C., Marsillac, S., Mokrani, A., 2002. Study of low temperature elaborated tailored optical band gap β-$In_2S_{3-3x}O_{3x}$ thin films. J. Cryst. Growth 235, 439–449.

Bhosale, R., Pujari, S., Muley, G., Pagare, B., Gambhire, A., 2013. Visible-light-activated nanocomposite photocatalyst of Cr_2O_3/SnO_2. J. Nanostruct. Chem. 3, 46.

Bian, Z., Zhu, J., Wang, S., Cao, Y., Qian, X., Li, H., 2008. Self assembly of active Bi_2O_3/TiO_2 visible photocatalyst with ordered mesoporous structure and highly crystallized anatase. J. Phys. Chem. C 112 (2008), 6258–6262.

Butler, M.A., Ginley, D.S., 1978. Prediction of flatband potentials at semiconductor-electrolyte interfaces from atomic electronegativities. J. Electrochem. Soc. 125, 228–232.

Casey, V., Stephenson, M.L., 1990. A study of undoped and molybdenum doped, polycrystalline, tin oxide thin films produced by a simple reactive evaporation technique. J. Phys. D Appl. Phys. 23, 1212–1215.

Chae, W.-S., Ko, J.-H., Choi, K.-H., Jung, J.-S., Kim, Y.-R., 2010. Photocatalytic efficiency analysis of CdS nanoparticles with modified electronic states. J. Anal. Sci. Technol. 1, 25–29.

Charitidis, C., Patsalas, P., Logothetidis, S., 2005. Optical and mechanical performance of nanostructured cerium oxides for applications in optical devices. J. Phys.: Conf. Ser. 10, 226–229.

Cheng, B., Russell, J.M., Shi, W., Zhang, L., Samulski, E.T., 2004. Large-scale, solution-phase growth of single-crystalline SnO_2 nanorods. J. Am. Chem. Soc. 126, 5972–5973.

Chopra, K.L., Major, S., Pandya, D.K., 1983. Transparent conductors—a status review. Thin Solid Films 102, 1–46.
Chun-Ming, L., Li-Mei, F., Xiao-Tao, Z., Wei-Lie, Z., 2007. The influence of nickel dopant on the microstructure and optical properties of SnO_2 nano-powders. Chin. Phys. 16, 95–99.
Couselo, N., Garcia Einschlag, F.S., Candal, R.J., Jobbagy, M., 2008. Tungsten-doped TiO_2 vs pure TiO_2 photocatalysts: effects on photobleaching kinetics and mechanism. J. Phys. Chem. C 112, 1094–1100.
Derbal, A., Omeiri, S., Bouguelia, A., Trari, M., 2008. Characterization of new heterosystem $CuFeO_2/SnO_2$ application to visible-light induced hydrogen evolution. Int. J. Hydrogen Energy 33, 4274–4282.
Elaziouti, A., Laouedj, N., Bekka, A., 2012. Synthesis, characterization and UV-A light photocatalytic activity of 20 wt% SrO–$CuBi_2O_4$ composite. Appl. Surf. Sci. 258, 5010–5024.
Fernandez, J., Kiwi, J., Lizama, C., Freer, J., Baeza, J., Mansilla, H.D., 2002. Factorial experimental design of Orange II photocatalytic decolouration. J. Photochem. Photobiol. A-Chem. 151, 213–221.
Foletto, E.L., Battiston, S., Collazzo, G.C., Bassaco, M.M., Mazutt, M.A., 2012. Degradation of leather dye using CeO_2–SnO_2 nanocomposite as photocatalyst under sunlight. Water Air Soil Pollut. 223, 5773–5779.
Frame, F.A., Carroll, E.C., Larsen, D.S., Sarahan, M., Browningb, N.D., Osterloh, F.E., 2008. First demonstration of CdSe as a photocatalyst for hydrogen evolution from water under UV and visible light. Chem. Commun. 2008, 2206–2208.
Fujishima, A., Honda, K., 1972. Electrochemical photolysis of water at a semiconductor electrode. Nature 238, 37–38.
Fumiaki, A., Eri, I., Akira, Y., 2013. Effect of particle size on the photocatalytic activity of WO_3 particles for water oxidation. J. Phys. Chem. C 117, 22584–22590.
Geng, J.Q., Jiang, Z.Y., Wang, Y.B., Yang, D., 2008. Carbon-modified TiO_2 nanotubes with enhanced photocatalytic activity synthesized by a facile wet chemistry method. Scr. Mater. 59, 352–355.
Gurlo, A., 2006. Interplay between O_2 and SnO_2: oxygen ionosorption and spectroscopic evidence for adsorbed oxygen. Chem. Phys. Chem. 7, 2041–2052.
Hou, L.-R., Yuan, C.-Z., Peng, Y., 2007. Synthesis and photocatalytic property of SnO_2/TiO_2 nanotubes composites. J. Hazard. Mater. B 139, 310–315.
Hyeong, J.Y., Hyunjoo, L., Nam, D.K., David, M.L., Sungju, Y., Jongheop, Y., 2011. A combination of two visible-light responsive photocatalysts for achieving the z-scheme in the solid state. ACS Nano 5, 4084–4090.
Iwase, A., Ng, Y.H., Ishiguro, Y., Kudo, A., Amal, R., 2011. Reduced graphene oxide as a solid-state electron mediator in z-scheme photocatalytic water splitting under visible light. J. Am. Chem. Soc. 133, 11054–11057.
Karunakaran, C., Panneerselvam, S.M., Gomathisankar, P., 2009. Photoreduction of chromium(VI) on ZrO_2 and ZnS surfaces. Monatsh. Chem. 140, 1269–1274.
Kim, Y.I., Atherton, S.J., Brigham, E.S., Mallouk, T.E., 1993. Sensitized layered metal oxide semiconductor particles for photochemical hydrogen evolution from nonsacrificial electron donors. J. Phys. Chem. 97, 11802–11810.
Kovalenko, M.V., Bodnarchuk, M.I., Stroyuk, A.L., Kuchmii, S.Y., 2004. Spectral, optical, and photocatalytic characteristics of quantum-sized particles of CdTe theo. Exp. Chem. 40, 220–225.
Li, L., Yan, B.J., 2009. CeO_2–Bi_2O_3 nanocomposite: two step synthesis, microstructure and photocatalytic activity. J. Non-Cryst. Solids 355, 776–779.
Li, H., Liua, G., Duana, X., 2009. Monoclinic $BiVO_4$ with regular morphologies: hydrothermal synthesis, characterization and photocatalytic properties. Mater. Chem. Phys. 115, 9–13.
Lin, X., Huang, F., Xing, J., Wang, W., Xu, F., 2008. Heterojunction semiconductor $SnO_2/SrNb_2O_6$ with an enhanced photocatalytic activity: the significance of chemically bonded interface. Acta Mater. 56, 2699–2705.
Liu, R., Ye, H., Xiong, X., Liu, H., 2010a. Fabrication of TiO_2/ZnO composite nanofibers by electrospinning and their photocatalytic property. Mater. Chem. Phys. 121, 432–439.
Liu, W., Chen, S., Zhang, S., Zhao, W., Zhang, H., Yu, X., 2010b. Preparation and characterization of p–n heterojunction photocatalyst p-$CuBi_2O_4$/n-TiO_2 with high photocatalytic activity under visible and UV light irradiation. J. Nanopart. Res. 12, 1355–1366.
Lu, X., Li, X., Chen, F., Ni, C., Chen, Z., 2009. Hydrothermal synthesis of prism-like mesocrystal CeO_2. J. Alloys Compd. 476, 958–962.
Magesh, G., Viswanathan, B., Viswanathan, R.P., Varadarajan, T.K., 2009. Photocatalytic behavior of CeO_2–TiO_2 system for degradation of methylene blue. Indian J. chem. 48A, 480–488.
Masami, N., Souta, H., Yasufumi, M., Yoshio, No., 2013. Enhanced photocatalytic activity of $BiVO_4$ by co-grafting of metal ions and combining with $CuBi_2O_4$. J. Photochem. Photobiol. A: Chem. 262, 52–56.
Mohamed, R.M., Aazam, E.S., 2012. Photocatalytic oxidation of carbon monoxide over NiO/SnO_2 nanocomposites under UV irradiation. J. Nanotechnol. 2012, 1–9.
Mora-Sero, I., Bisquert, J., Dittrich, T., Belaidi, A., Susha, A.S., Rogach, A.L., 2007. Photosensitization of TiO_2 layers with CdSe quantum dots: correlation between light absorption and photoinjection. J. Phys. Chem. C 111, 14889–14892.
Mukhpadhyay, A.K., Mitra, P., Chatterjee, A.P., Maiti, H.S., 2000. Tin dioxide thin film gas sensor. Ceram. Int. 26, 123.
Nathan, T.H., Holmberg, C.V., Korgel, B.A., Mullins, C.B., 2012. Electrochemical synthesis and characterization of p-$CuBi_2O_4$ thin film photocathodes. J. Phy. Chem. C 116, 6459–6466.
Nayral, C., Viala, E., Collière, V., Fau, P., Senocq, F., Maisonnat, A., Caudret, B., 2000. Synthesis and use of a novel SnO_2 nanomaterial for gas sensing. Appl. Surf. Sci. 2000 (164), 219–226.
Park, Y.R., Kim, K.J., 2003. Sputtering growth and optical properties of [100]-oriented tetragonal SnO_2 and its Mn alloy films. J. Appl. Phys. 94, 6401.
Pullar, R.C., Taylor, M.D., Bhattacharya, A.K., 1988. The manufacture of yttrium aluminium garnet (YAG) fibres by blow spinning from a sol-gel precursor. J. Europ. Cer. Soc. 18, 1759–1764.
Rakhshani, A.E., Makdisi, Y., Ramazaniyan, H.A., 1998. Electronic and optical properties of fluorine- doped tin oxide films. J. Appl. Phys. 83, 1049–1057.
Rengaraj, S., Kezhen, Q., Al-Kindy, S.M.Z., Mika, S., Younghun, K., Tai, C.-W., 2014. A simple hydrothermal route for the preparation of HgS nanoparticles and their photocatalytic activities. RSC. Adv. 4, 15371–15376.
Sangami, G., Dharmaraj, N., 2012. UV–visible spectroscopic estimation of photodegradation of rhodamine-B dye using tin(IV) oxide nanoparticles. Spectr. Chim. Acta Part A: Mol. Biomol. Spect. 97, 847–852.
Sasahara, A., Pang, C.L., Onishi, H., 2006. Local work function of Pt clusters vacuum-deposited on a TiO_2 surface. J. Phys. Chem. B 110, 17584–17588.
Sasaki, Y., Iwase, A., Kato, H., Kudo, A., 2008. The effect of co-catalyst for Z-scheme photocatalysis systems with an Fe^{3+}/Fe^{2+} electron mediator on overall water splitting under visible light irradiation. J. Cat. 259, 133–137.
Sasaki, Y., Nemoto, H., Saito, K., Kudo, A., 2009. Solar water splitting using powdered photocatalysts driven by z-schematic inter-particle electron transfer without an electron mediator. J. Phys. Chem. C 113, 17536–17542.
Sasikala, R., Shirole, A., Sudarsan, V., et al, 2009. Highly dispersed phase of SnO_2 on TiO_2 nanoparticles synthesized by polyol-mediated route: photocatalytic activity for hydrogen generation. Int. J. Hydrogen Energy 34, 3621–3630.

Seiji, K., Toshiyuki, A., 2009. Photocatalysis for water oxidation by Fe_2O_3 nanoparticles embedded in clay compound: correlation between its polymorphs and their photocatalytic activities. J. Mater. Sci. 44, 2890–2898.

Shen, J., Cortright, R.D., Chen, Y., Dumesic, J.A., 1994. Microcalorimetric and infrared spectroscopic studies of γ-Al_2O_3 modified by tin oxides. Catal. Lett. 26 (1994), 247–257.

Sikong, L., Kongreong, B., Kantachote, D., Sutthisripok, W., 2010. Photocatalytic activity and antibacterial behavior of Fe^{3+}-doped TiO_2/SnO_2 nanoparticles. Energy Res. J. 1, 120–125.

Teegarden, K., 1966. Halide lattices. Luminescence and in-organics solids, 53–118.

Teeramongkonrasmee, A., Sriyudthsak, M., 2000. Methanol and ammonia sensing characteristics of sol–gel derived thin film gas sensor. Sens. Actuators B Chem. 66, 256–259.

Vasanth Kumar, K., Porkodi, K., Rocha, F., 2008. Langmuir-Hinshelwood kinetics – a theoretical study. Catal. Commun. 9, 82–84.

Vora, J.J., Chauhan, S.K., Parmar, K.C., Vasava, S.B., Sharma, S., Bhutadiya, L.S., 2009. Kinetic study of application of ZnO as a photocatalyst in heterogeneous medium. E-J. Chem. 6, 531–536.

Wang, C., Zhao, J., Wang, X., Mai, B., Sheng, G., Peng, P., Fu, J., 2002. Preparation, characterization and photocatalytic activity of nano-sized ZnO/SnO_2 coupled photocatalysts. Appl. Cat. B-Environ. 39, 269–279.

Wang, X., Lian, W., Fu, X., Basset, J.M., Lefebvre, F., 2006a. Structure, preparation and photocatalytic activity of titaniumoxides on MCM-41. J. Catal. 238, 13–20.

Wang, H.C., Li, Y., Yang, M., 2006b. Fast response thin film SnO''2 gas sensors operating at room temperature. Sens. Actuators B Chem. 119, 380–383.

Wang, Q.-Q., Lin, B.-Z., Xu, B.-H., Li, X.-Li., Chen, Z.-J., Pian, X.-T., 2010a. Preparation and photocatalytic properties of mesoporous SnO_2–hexaniobate layered nanocomposite. Microporous Mesoporous Mater. 130, 344–351.

Wang, Z., Li, Z., Sun, J., Zhang, H., Wang, W., Zheng, W., Wang, C., 2010b. Improved hydrogen monitoring properties based on p-NiO/n-SnO2 heterojunction composite nanofibers. J. Phys. Chem. C 114, 6100–6105.

Wang, C., Thompson, R.L., Ohodnicki, P., Baltrus, J., Matranga, C., 2011. Size-dependent photocatalytic reduction of CO_2 with PbS quantum dot sensitized TiO_2 heterostructured photocatalysts. J. Mater. Chem. 21, 13452–13457.

Xi, L., Qian, D., Tang, X., Chen, C., 2008. High surface area SnO_2 nanoparticles: synthesis and gas sensing properties. Mater. Chem. Phys. 108, 232–236.

Xiaoning, W., Jinping, J., Yalin, W., 2011. Degradation of C.I. Reactive Red 2 through photocatalysis coupled with water jet cavitation. J. Hazard. Mat. 185, 315–321.

Xie, Y., Yuan, C., Li, X., 2005. Photosensitized and photocatalyzed degradation of azo dye using Ln^{n+}-TiO_2 sol in aqueous solution under visible light irradiation. Mater. Sci. Eng., B 117, 325–333.

Xu, Y., Schoonen, M.A.A., 2000. The absolute energy positions of conduction and bands of selected semiconducting minerals. Amer. Mineral. 85, 543–556.

Yang, H., Ouyang, J., Tang, A., Xiao, Y., Li, X., Dong, X., 2006. Eletrochemical synthesis and photocatalytic property of cuprous oxide nanoparticles. Mater. Res. Bull. 41, 1310–1318.

Yang, H.Y., Yu, S.F., Cheng, C.W., Tsang, S.H., Liang, H.K., Fan, H.J., 2009. Randomly packed *n*-SnO_2 nanorods/*p*-SiC heterojunction light-emitting diodes. Appl. Phys. Lett. 95, 201104.

Yath, D.E., 1974. Healy, site-binding model of the electrical double layer at the oxide/water interface. J. Chem. Soc., Faraday Trans. 70, 1807–1818.

Ying, Z., Wan, Q., Song, Z.T., Feng, S.L., 2004. SnO2 nanowhiskers and their ethanol sensing characteristics. Nanotechnology 15, 1682.

Yongchuan, W., Xingxing, S., Feng, C., 2014. Improving the catalytic activity of CeO_2/H_2O_2 system by sulfation pretreatment of CeO_2. J. Mol. Cat. A: Chem. 381, 38–45.

Yu, J., Su, Y., Cheng, B., Zhou, M., 2008. Effects of pH on the microstructures and photocatalytic activity of mesoporous nanocrystalline titania powders prepared via hydrothermal method. J. Mol. Catal. A-Chem. 258, 104–112.

Zhang, C., Zhu, Y.F., 2005. Synthesis of square Bi_2WO_6 nanoplates as high-activity visible-light-driven photocatalysts. Chem. Mater. 17, 3537–3545.

Zhang, F., Zhao, J., Shan, T., Hidaka, H., Pelizzetti, E., Serpone, N., 1998. TiO_2-assisted photodegradation of dye pollutants: II. Adsorption and degradation kinetics of eosin in TiO_2, dispersions under visible light irradiation. Appl. Cat. B-Environ. 15, 147–156.

Zhang, L., Li, J., Chen, Z., Tang, Y., Yu, Y., 2006. Preparation of Fenton reagent with H_2O_2 generated by solar light-illuminated nano- Cu2O/MWNTs composites. Appl. Catal. A 299, 292–297.

Zhang, J., Xiong, Z., Zhao, X.S., 2011. Graphene–metal–oxide composites for the degradation of dyes under visible light irradiation. J. Mater. Chem. 21, 3634–3640.

Zhang, L., Zhang, H., Huang, H., Liu, Y., Kang, Z., 2012. Ag3PO4/SnO2 Semiconductor Nanocomposites with Enhanced Photocatalytic Activity and Stability. The Royal Society of Chemistry and The Centre National de la Recherche Scientifique.

Zhong, C., Xueqiang, C., Lixian, S., Yinghe, He., 2011. Photocatalytic activity of Bi_2O_3 prepared by different precipitants. Adv. Mat. Res. 239–242, 998–1001.

Zhuang, H.S., Xia, H.L., Zhang, T., Xiao, D.C., 2008. Synthesis, characterization, and visible-light photocatalytic activity of Fe_2O_3/SnO_2 nanocomposites. Mater. Sci-Poland 26, 517–526.